Article

Micromechanical Behavior of Granular Materials Caused by Particle Shapes under Triaxial Loading

Daraporn Phusing[1,a,*], Pulpong Pongvithayapanu[1,b], Udomporn Tungkasiri[1,c], and Porjan Tuttipongsawat[2,d]

1 Department of Civil Engineering, Faculty of Engineering at Sriracha, Kasetsart University, Chonburi 20230, Thailand
2 Department of Computer Science and Information, Faculty of Science at Sriracha, Kasetsart University, Chonburi 20230, Thailand
E-mail: [a,*]daraporn@eng.src.ku.ac.th (Corresponding author), [b]pulpong@eng.src.ku.ac.th, [c]udomporn@ku.th, [d]porjan@eng.src.ku.ac.th

Abstract. The mechanical behavior was investigated of 3 different particle shapes under different stress paths by setting various intermediate stress ratios. The method of 3D discrete element was applied to research the effect of particle shapes with aspect ratios of ellipsoids and spheres, with both specified by height/width values of 0.4, 0.6, and 1 under different intermediate stress ratios or b values. Each one was used with a single particle shape based on 16 different sizes and random rotation angles. All 3 samples were subjected to a limited isotropic pressure of 100 kPa prior to shearing and constant mean stress using a stress controller. Macro behavior was evaluated based on the stress and strain responses. Micro mechanisms were reported based on the coordination number together with the sliding contract fraction. The fabric tensor of the contact normal, normal contact, and tangential contact forces were examined for the various sample shapes during intermediate loadings of different stress ratios. It was found that anisotropic fabrics and the b values relative to the normal contact force were higher than for the contact normal for all shapes. Furthermore, at the peak stress of each stress path, the specific behavior of normal contact forces varied with the particle shape.

Keywords: Discrete element, particle shape, intermediate stress ratio, fabric, ellipsoids.

1. Introduction

The mechanical behavior of cohesionless soils is influenced by particle shape, confined pressure, density, and stress paths among other aspects [1-3]. It has been generally accepted that variation in strength and deformation of granular soil depends on its particle shape, which can be examined using laboratory experiments. For example, Cho et al. [4] used sand to study the effects of particle shape about the density and mechanical properties in various stresses and reported that increased particle deformity increased the critical state angle of the shear strength. In addition, Carvaretta et al. [2] used a mixture of spherical and angular glass beads with sand. They found various types of particle shape behavior at the critical state and that liquefaction ability was highly affected by the shape of the particles at the critical state. Even though the experiment's objective was to investigate the influence of particle shape, the particle shape mechanism was examined from other perspectives and using other methods. The behavior of granular soil was different, depending on the formation under different stress paths, where the major σ_1, the intermediate σ_2, and the minor σ_3 stresses were varied. Other experiments and simulation studies using DEMs reported that the intermediate stress ratio or the b values (where b = $(\sigma_2-\sigma_3)/(\sigma_1-\sigma_3)$) influenced the behavior of granular soil [8–10]. Lade [5] found that the shearing resistance ϕ angle increased from $b = 0$ and displayed various trends, depending on the sand's type. Xiao et al. [6] conducted triaxial tests using coarse sand and reported that b played a significant role in the critical state line. However, the experiments presented limited information of the macro strength and deformation behaviors of granular materials. Micro data of the assemblies requires highly technological methods, such as CT scanning, photoelasticity, and X-rays, among others. In addition, it is not possible to prepare similar assemblies in laboratory tests. Computer simulations have been used to avoid the confounding effects from using different samples and testing conditions in individual experiments as well as being less highly technological. A DEM [7] was the main tool used to discover the effect of b to both the macro and micro mechanical responses of granular soils [8, 10-16]. Oda [8] conducted a drained triaxial compression test on a sample of sand and showed that the distribution of contact orientation was equal in an equal area stereo net, for the isotropic compression state. However, it had to be reoriented under deviatoric loading to maximize the contact density in directions close to that of maximum principal stress. Bathurst [9] used the data of Oda [8] to determine some contacts under similar orientations using the statistical average technique and replotting the contact density in every orientation interval. This result showed that the magnitude of contact anisotropy increased in the direction of major principal stress. Zhou et al. [15] reported the evolution of micro responses spherical particles for $b = 0$, 0.25, 0.5, 0.7, and 1. Their results showed that the anisotropic mechanics had the same trends as deviatoric stress and fabric tensors.

Nouguier et al. [17] used biaxial simulation with different (isotropic polygonal, elongate polygonal and circular) shapes and showed that the unrelation of behaviors of isotropic particles samples and those of the anisotropic particle samples. Additionally, Xie et al. [18] used DEMs to simulate 3 particle shapes with different aspect ratios, including spheres, and reported those different aspect ratios and the intermediated stress ratio, b, influenced the stress-strain curve, the shearing resistance angle, and the fabric structure at the critical state. In addition, Liu et al. [16] used DEMs to create isotropic assemblies with different densities and found that the deviatoric fabric was dependent on the shear mode. These various research studies used spherical particles and other shapes to report the effect of mainly macro behavior. However, the data regarding the microscopic (such as contact forces chain and anisotropic coefficient) behavior of the contact of different particle shapes has been only analyzed within a narrow scope. Most studies have used a simple stress path, in contrast to the real-world case. The real stress path has true triaxial loading, in which different intermediated stress ratios of b are categorized. Therefore, the current study aimed to review the macro behavior of 3 samples using different particle shapes under different intermediated stress ratios ($b = 0$, 0.3, 0.5, 0.7, and 1). At the same time, the micro mechanisms were investigated of normal and tangential contact force chains, the anisotropic coefficient of the contact normal forces, contact tangential forces, and the contact orientation of each particle shape and b stress path.

2. Simulation Details

2.1. Particle Characteristics and Sample Preparation

To review the particle shape's effect, the researcher created 3 particle shapes with height-width aspect ratios of 0.4, 0.6, and 1 mm, where the aspect ratios of 0.4 and 0.6 were ellipsoidal particles and the ratio of 1 was a sphere. Figure 1(a) shows the geometrical sizes, where vector a is the central axis. Figure 1(b) shows the orientation angles of γ_1 and γ_2 randomly set from 0 to 90 degrees and from 0 to 360 degrees, respectively. Samples were created by using 8,000 particles of a single particle shape with 16 different widths in space. The widths of the particles varied from 3 to 4.5 mm: 3 mm (557), 3.1 mm (486), 3.2 mm (489), 3.3 mm (506), 3.4 mm (527), 3.5 mm (486), 3.6 mm (482), 3.7 mm (481), 3.8 mm (507), 3.9 mm (491), 4.0 mm (502), 4.1 mm (502), 4.2 mm (503), 4.3 mm (496), 4.4 mm (515), and 4.5 mm (470), where the numbers in the parentheses refer to the number of particles in each width.
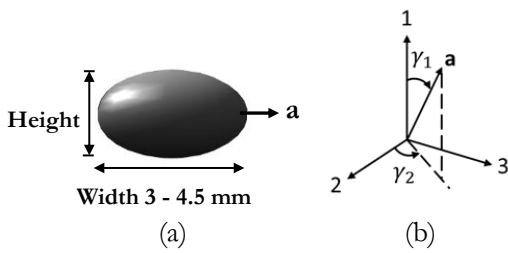
Fig. 1. (a) particle shape; (b) orientation angle where vector a is the central axis of revolution of the oval (after Kuhn [19]).

Table 1 shows the aspect ratios, sizes, and void ratios of the samples before shearing. Figures 2(a)–(c) show the spherical particles, where the aspect ratio is h/w = 1 and the ellipsoidal particles, where the aspect ratios are h/w =

0.6 and h/w = 0.4, respectively, after isotropic compression force was applied until 100 kPa using a periodic boundary.

Table 1. Particle shapes and sample data.

Shape	Aspect Ratio	Sample size (cm)	Void ratio
	h/w = 1	7.1 × 7.1 × 7.1	0.57
	h/w = 0.6	6.07 × 5.76 × 5.76	0.424
	h/w = 0.4	5.0 × 5.05 × 4.95	0.44

(a)   h/w = 1   (b)   h/w = 0.6   (c)   h/w = 0.4
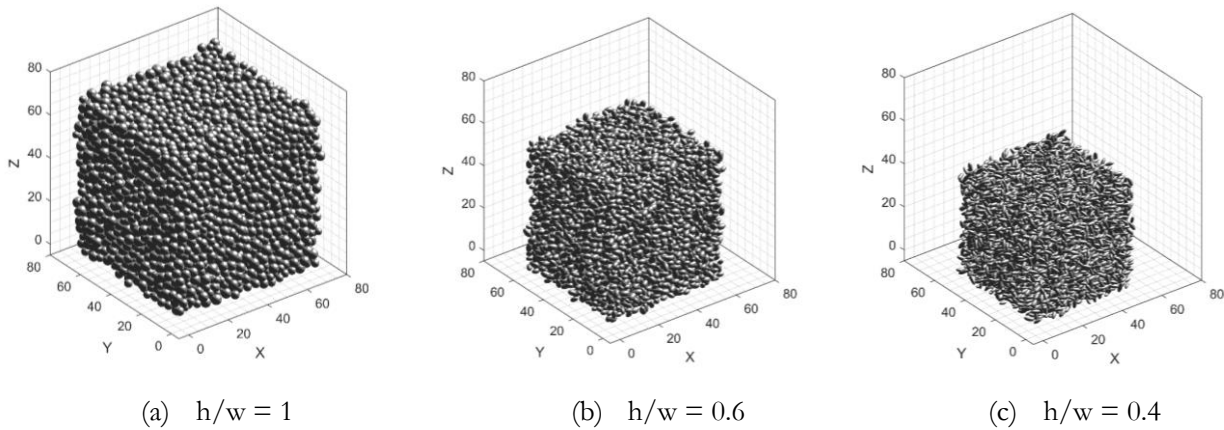
Fig. 2. Samples after isotropic compression (a) spherical particle sample (h/w = 1); (b) ellipsoidal particle sample (h/w = 0.6); (c) (h/w = 0.4).

2.2. Simulation Data

Figure 3 shows an image of the stress paths projected onto a normalized π-plane, where b = 0, 0.3, 0.5, 0.7, and 1. This study used a DEM code called Oval created by Kuhn [19]. The parameters run in Oval were mass density (2,650 kg/(m³)), normal and tangential stiffness (1×106 N/m), friction coefficient (0.5), and damping (0.05). The small stress rate was used to obtain the small strain rate under stress control and constant mean stress in all stress paths. The unbalanced force index (0.1%) was limited and the simulation was completed close to a quasi-static state [19].
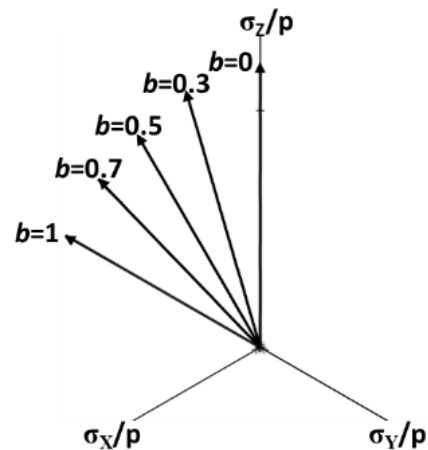

Fig. 3. Simulation stress paths b = 0, 0.3, 0.5, 0.7 and 1 on the normalized π-plane.

3. Results

3.1. Stress-Strain Relationship

Figures 4(a)–(c) show the relationship of the stress ratio (q/p), equivalent deviatoric strain ε_d (%), and volumetric strain ε_v (%) in all shapes and tests, where the deviatoric stress can be expressed as:

$$q = \sqrt{\frac{1}{2}\left\{(\sigma_x - \sigma_y)^2 + (\sigma_y - \sigma_z)^2 + (\sigma_x - \sigma_z)^2\right\}} \quad (1)$$

and the mean stress as:

$$p = \frac{1}{3}(\sigma_x + \sigma_y + \sigma_z) \quad (2)$$

where σ_z, σ_x, and σ_y are the vertical stress (stress in the Z direction) and the horizontal stresses (stress in directions of the X and Y axes, respectively), as shown in Fig. 3. The volumetric strain can be expressed as:

$$\varepsilon_v = \frac{dv}{v} \quad (3)$$

where dv is the volume change of the sample and v is the volume before shearing. The equivalent deviatoric strain can be expressed as:

$$\varepsilon_d = \sqrt{\frac{2}{3}\left\{(\varepsilon_x - \varepsilon_y)^2 + (\varepsilon_y - \varepsilon_z)^2 + (\varepsilon_x - \varepsilon_z)^2\right\}} \quad (4)$$

where ε_z, ε_x, and ε_y are the vertical strain (in the Z direction) and the two horizontal strains (in directions of the X and Y axes, respectively). Figures 4(a)–(c) show that the stress ratio (q/p) and the equivalent deviatoric strain (ε_d as a %) of the ellipsoid h/w = 0.4 had the highest shear stress, followed by h/w = 0.6, with the sphere h/w = 1 having the smallest. These results were the same as those presented by Xie et al. [18]. The sphere h/w = 1 and the ellipsoidal particle samples h/w = 0.6 and 0.4 all showed the nonlinear development of volumetric strain ε_v (%), depending on the b values in Figs. 4(a)–(c). For the spherical particle sample in Fig. 4(a), the volumetric strain ε_v became dilated when the stress ratio increased. Similar results were reported from using the DEM with one constant b value by Thornton [20], Kuhn [21], and Wang et al. [23], among others, which was different from the spherical particle sample. The ellipsoidal particles in both samples show compression and dilation as in Figs. 4(b) and (c), respectively. These results implied that the spherical particle sample was dense in all directions (Z, X, and Y) after isotropic compression. In Figs. 4(b) and (c) where the ε_v of stress path b = 0 of the ellipsoidal particle samples and h/w = 0.6 and 0.4 where $\sigma_z > \sigma_x = \sigma_y$, the ε_v ($= \varepsilon_x + \varepsilon_y + \varepsilon_z$) shows (positive) compression because the summary of dilation $\varepsilon_x + \varepsilon_y$ was less than the compression ε_z. Therefore, ε_v shows compression,

indicating ellipsoidal particle samples with inherent anisotropy. This inherent anisotropy was caused by the loading in the vertical direction (direction Z) being higher than in the other 2 horizontal ones (directions X and Y). The inherent anisotropy in the micro data is explained in the Microscopic Results section below.

3.2. Microscopic Behavior

Figures 5(a)–(c) show the graphs of the coordination number and ε_d (%) with different b values for all shapes, where the ellipsoidal particle samples (h/w = 0.6 and 0.4) have coordination numbers of 9.28 and 9.58, respectively, before shearing, whereas the spherical shape (h/w = 1) has a value of 5.67. This corresponded to the higher strength of the ellipsoidal particle sample than the spherical particle sample because of closer contacts within the sample. The greater coordination number shows more contacts that increase the load carrying capacity. In addition, Fig. 9 shows that the coordination number does not depend on the b values in spherical particle sample, where it does depend on the b values in ellipsoidal particles (h/w = 0.6 and 0.4). Furthermore, the coordination number depended on the particle type. Figures 6(a)–(c) show the graphs of the sliding contact fraction and, the graph of ε_d for the different b values in all shapes. These figures show that the ellipsoidal particle sample (h/w = 0.4) had more sliding particles than the ellipsoidal particle sample (h/w = 0.6) and the spherical particle sample (h/w = 1), when the deviatoric stress increased.

3.3. Microscopic Characteristics

In Figs. 7 (a) and (b), the normal contact force (f_n^c)'s direction is normal to the tangential contact force (f_t^c) in the contact plane at the point of contact of two particles where both are either spherical or ellipsoidal. During shearing, the particle orientation and contact forces (f^c) continuously changed. This study focused on the normal and tangential contact forces. Figures 8(a1)–(a3) show the chains of normal, and tangential contact forces of spherical, h/w = 1, and ellipsoidal samples, h/w = 0.6 and 0.4, after isotropic compression of 100 kPa. Figures 9(a1)–(c3) shows at peak stress of b = 0 but Figs. 10(a1)–(c3) shows at peak stress of b = 1. In these figures, the line indicates one contact force and the colors in each line correspond to the intensity of contact force. Figures 8(a1)–(a3) show that the normal contact forces are symmetrical distribution in all directions of all shapes. Nevertheless, the particle h/w=0.6 in Fig. 8(a2) shows higher intensity than h/w = 1 (sphere) and h/w = 0.4 at isotropic compression 100 kPa. This result shows that different normal contact forces depend on the particle shape. Figures 9(a1)–(a3) show that the normal contact forces align with the vertical axis at peak stress under b = 0. Besides, the normal contact force of the particle h/w = 0.6 shows the highest intensity followed by h/w = 0.4 and h/w = 1. Then, Fig. 9(b1) shows that the h/w = 0 sample shows almost zero tangential contact forces at peak stress

at $b = 0$, h/w = 0.6 shows the highest direction of 45 degrees and h/w = 0.4 shows the highest direction (higher than 45 degrees). Then, Figs. 10(a1)–(b3) show the normal, tangential contact forces of particle h/w = 1, 0.6 and 0.4 at peak stress under $b = 1$. Figures 10(a1)–(a3) shows that the normal contact force of the particle h/w = 0.6 has higher values than h/w = 0.4. And h/w = 1 has the smallest values similar to stress $b = 0$ in Figs. 9(a1)–(a3). Nevertheless, the normal contact force when stress path $b = 0$ is greater than stress path $b = 1$. To conclude, the normal and tangential contact forces show dependency on the shape of particles and b. In Figs. 9 and 10, the normal and tangential contact forces at peak stress show changes

according to the reorientation and the change of contact force's intensity. When stress path is $b = 0$, σ_z is at the maximum peak. The reorientation of particles causes the orientation of contact forces of increasing load-carrying capacity to resist σ_z increase. At the same time, if stress path is $b = 1$, σ_x and σ_y increase causes the particle reorientation to resist the stress in σ_x and σ_y. Therefore, the direction of major principal stress and loss of the minor one has influence on the orientation of contact forces, depending on the particle's shape.
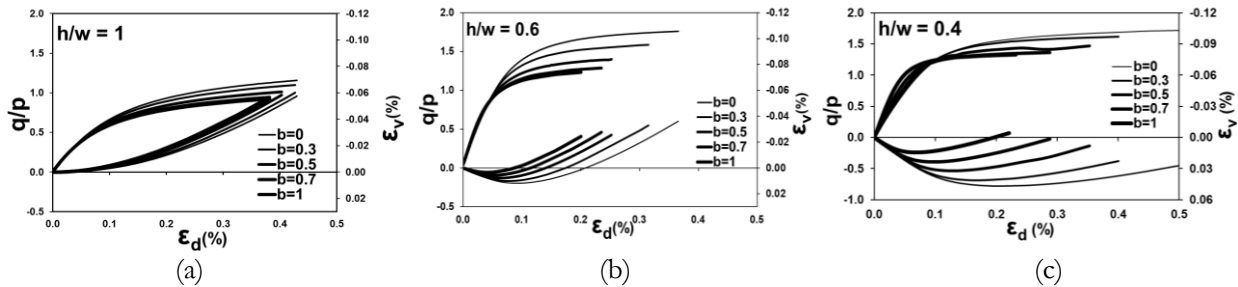

Fig. 4. Stress-strain relationship of stress paths $b = 0$, 0.3, 0.5, 0.7 and 1: (a) h/w=1, (b) h/w=0.6 and (c) h/w=0.4.
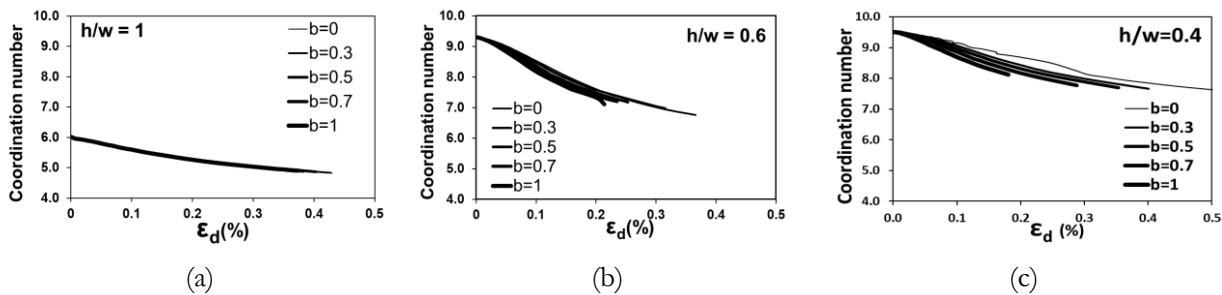

Fig. 5. Graph of coordinate number and ε_d (%) under different b of all samples.
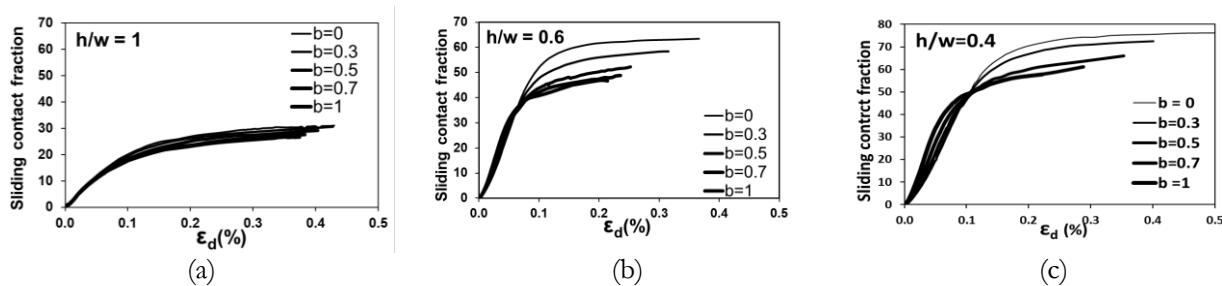

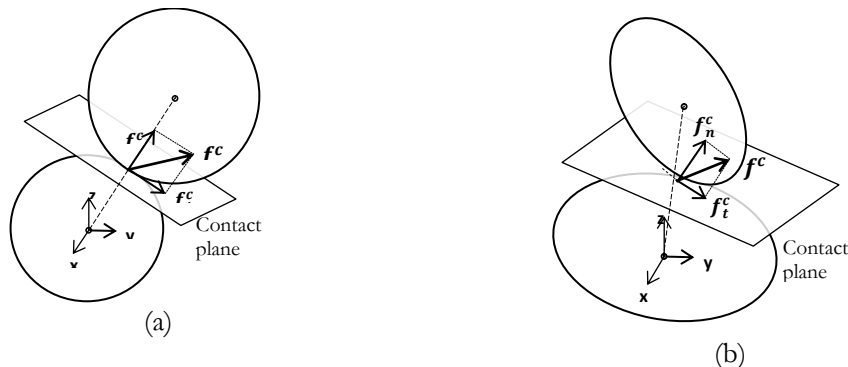Fig. 6. Graphs of sliding contact fraction and ε_d (%) under different b of all samples.

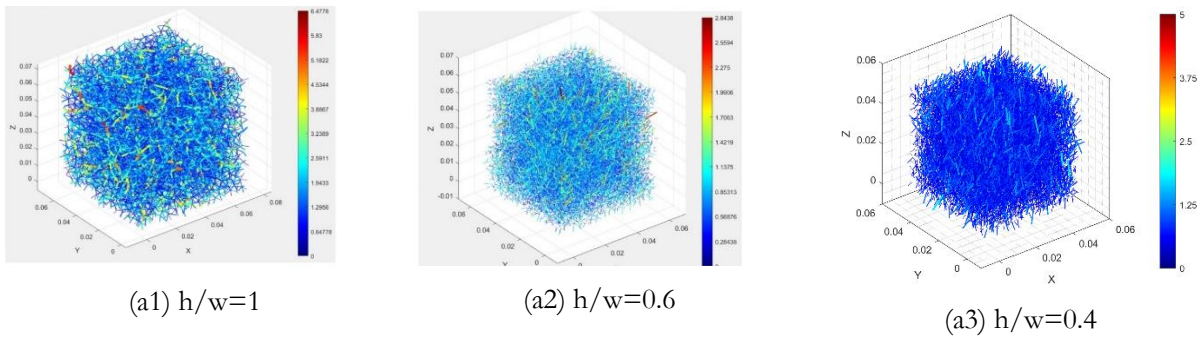Fig. 7. Interparticle contact forces; (a) spherical particles; (b) ellipsoidal particles.

| (a1) h/w=1 | (a2) h/w=0.6 | (a3) h/w=0.4 |

Fig. 8. (a1) - (a3) The chains of contact normal of h/w = 1, 0.6 and 0.4 after isotropic compression 100 kPa.

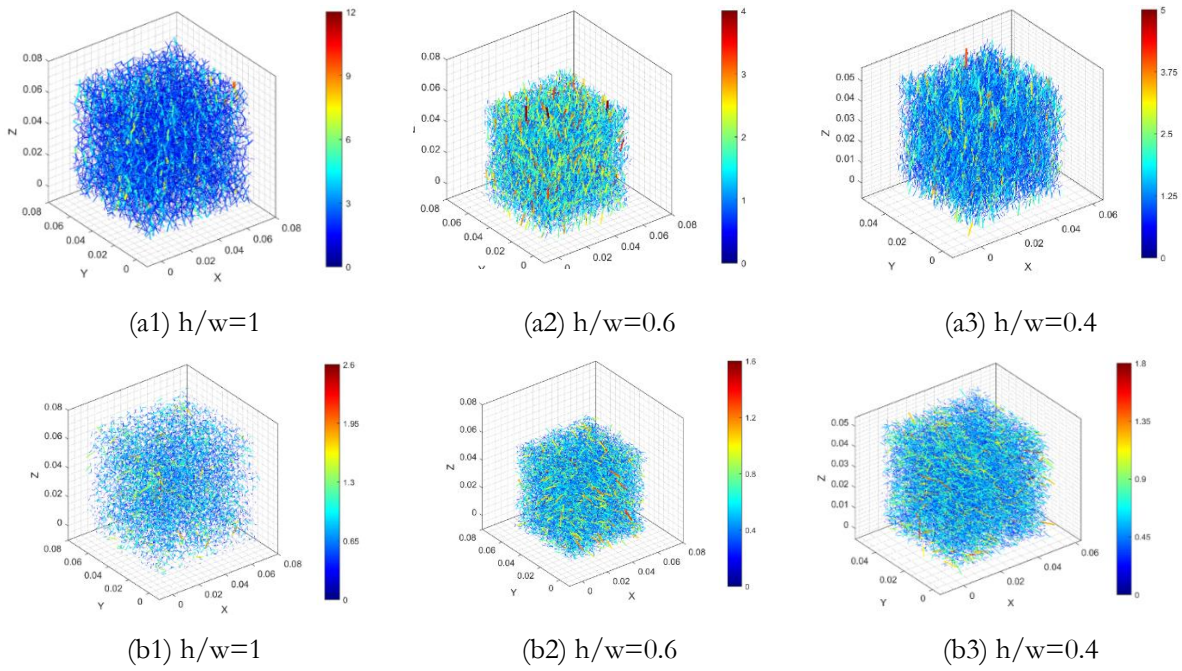| (a1) h/w=1 | (a2) h/w=0.6 | (a3) h/w=0.4 |

| (b1) h/w=1 | (b2) h/w=0.6 | (b3) h/w=0.4 |

Fig. 9. (a1) - (a3) The chains of normal contact forces and (b1-b3) the chains of tangential forces at peak stress of sample h/w=1, 0.6 and 0.4 at peak of $b = 0$.
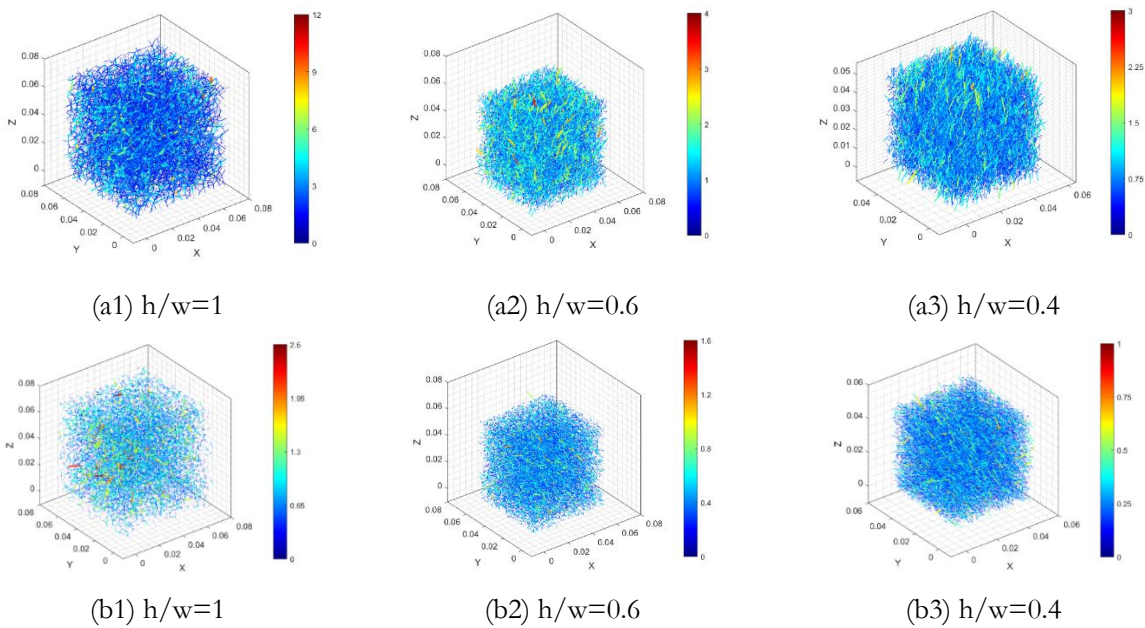

| (a1) h/w=1 | (a2) h/w=0.6 | (a3) h/w=0.4 |

| (b1) h/w=1 | (b2) h/w=0.6 | (b3) h/w=0.4 |

Fig. 10. (a1) - (a3) The chains of normal contact forces and (b1-b3) the chains of tangential forces at peak stress of sample h/w=1, 0.6 and 0.4 at peak of $b = 1$.

3.4. Contact Distribution

Figures 11(a1)–(c9) show contact intensity distribution referred from Figs. 10(a1)–(a3) of normal contact forces before shearing in stress paths $b = 0$ and $b = 1$ for h/w = 1 (spheres), h/w = 0.6 and 0.4 (ellipsoids). The length of each direction shows the contact intensity in each direction of the principal stresses. The color represents the magnitude of contact in each direction. It can be seen in Fig. 11(a1) that the normal contact forces of spherical particle h/w = 1 are distributed in isotropic after isotropic compression but those of the ellipsoidal particle h/w = 0.6 and 0.4 are not. Figure 11(a2) shows that most of the normal contact forces of h/w = 0.6 seem aligned with the vertical loading direction (σ_z) and greater than the other two horizontal symmetry directions (σ_x and σ_y) with few and small normal contact forces. In Fig. 11(a3), the normal contact forces of h/w = 0.4 are asymmetric in all directions. The normal contact forces of h/w = 0.4 are aligned with the vertical loading direction (σ_z) in the same level of intensity inclined 0 to 45 degrees from vertical directions. The normal contact force

distribution shows the mechanical picture of contact forces and its anisotropic [15]. The normal contact forces at a peak stress of stress path $b = 0$ and $b = 1$ in all shapes are shown in Figs. 11(b1)–(c3) referring from the force chain of the normal contact forces in Figs. 8(b1)–(c3). It can be seen in Figs. 11 (b1) - (b3) that the great magnitude and intensity of the normal contact forces are in vertical direction where loading direction (σ_z) is in the maximum when $b = 0$. In addition, Figs. 11(c1)–(c3) show that when $b = 1$ ($\sigma_z = \sigma_x$), the magnitude and intensity of the normal contact forces in vertical (σ_z) and horizontal (σ_x) directions are greater than those in horizontal (σ_y) directions. Moreover, in Fig. 11(c1), the normal contact forces of vertical (σ_z) direction seem equal to the magnitude with horizontal (σ_x) direction when h/w = 1 (spheres). But the normal contact forces of vertical (σ_z) direction are greater than those in horizontal (σ_x) direction when h/w = 0.6 and 0.4 in Figs. 11(c2) and (c3). All of these result from the fact that the sample of h/w = 1 is isotropic but h/w = 0.6 and 0.4 are anisotropic before shearing.

(a1) h/w =1, before shearing.　　(a2) h/w =0.6, before shearing.　　(a3) h/w =0.4, before shearing.

(a4) h/w =1, at peak of $b = 0$.　　(a5) h/w =0.6, at peak of $b = 0$.　　(a6) h/w =0.4, at peak of $b = 0$.

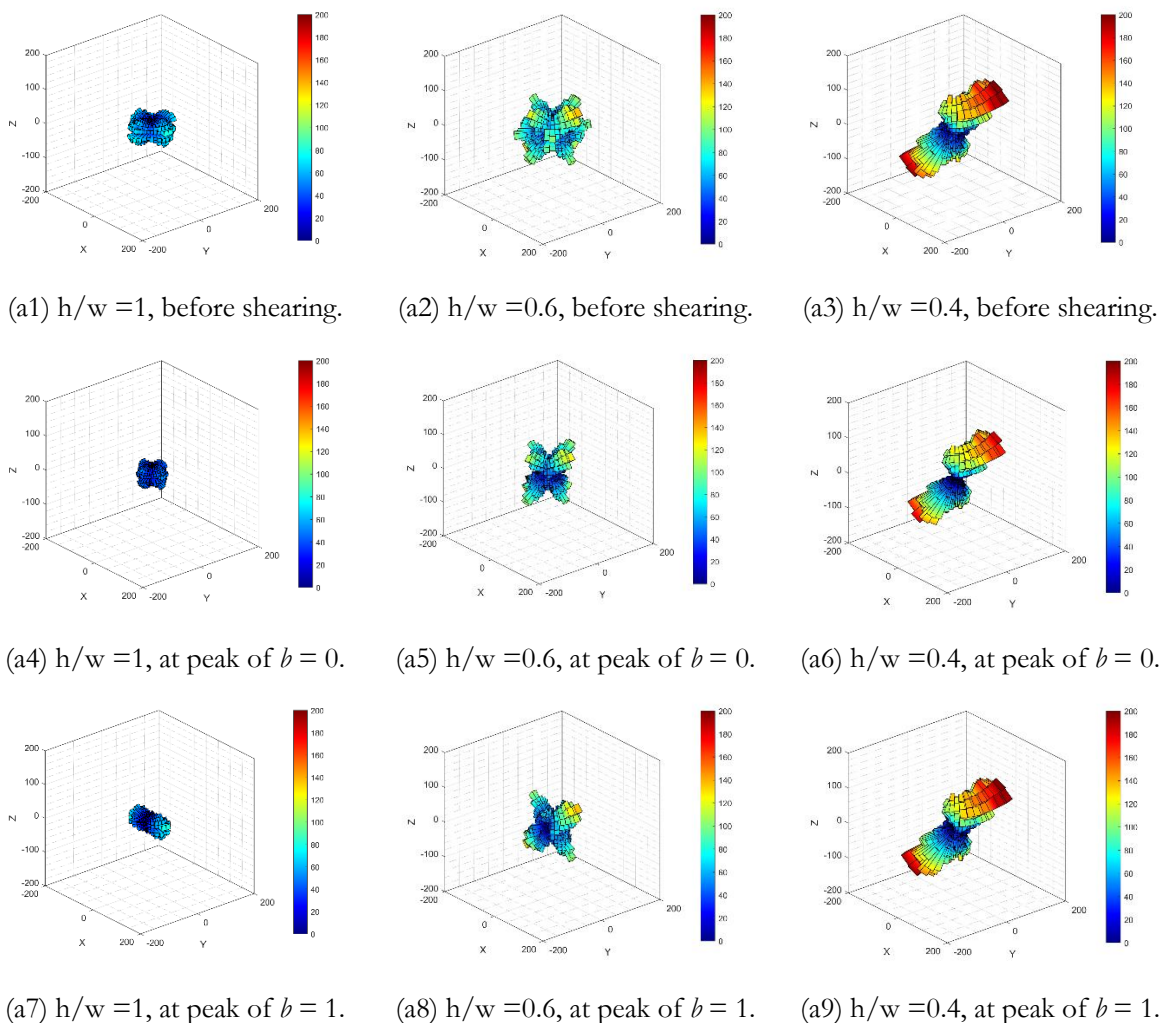(a7) h/w =1, at peak of $b = 1$.　　(a8) h/w =0.6, at peak of $b = 1$.　　(a9) h/w =0.4, at peak of $b = 1$.

Fig. 11. (a1) – (a9) Contact normal distributions in all shapes: (a1-a3) before shearing before shearing, (a4-a6) at peak of $b = 0$, and (a7-a9) at peak of $b = 1$.
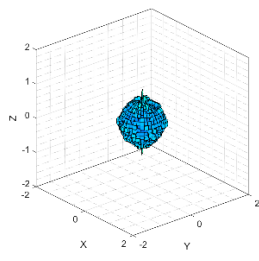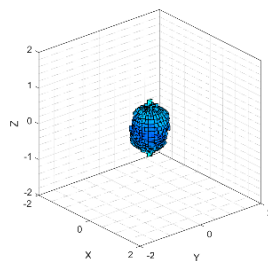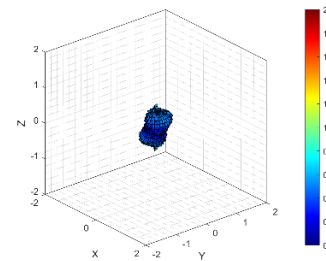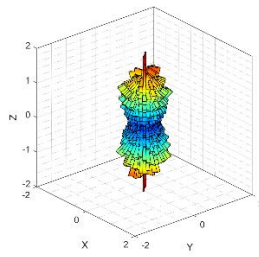
(b1) h/w =1, before shearing   (b2) h/w =0.6, before shearing   (b3) h/w =0.4, before shearing
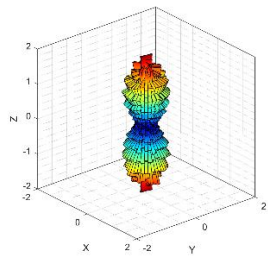
(b4) h/w =1, at peak of $b = 0$.   (b5) h/w =0.6, at peak of $b = 0$.   (b6) h/w =0.4, at peak of $b = 0$.
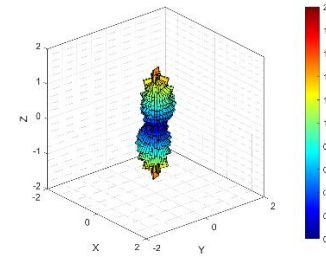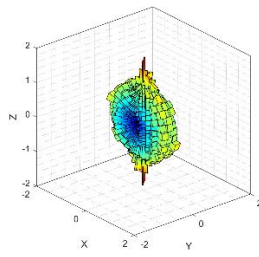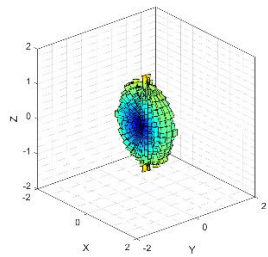
(b7) h/w =1, at peak of $b = 1$.   (b8) h/w =0.6, at peak of $b = 1$.   (b9) h/w =0.4, at peak of $b = 1$.
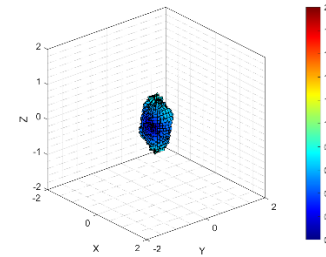
Fig. 11. (b1) - (b9) Normal contact forces distributions in all shapes: (b1) - (b3) before shearing before shearing, (b4) –(b6) at peak of $b = 0$, and (b7) - (b9) at peak of $b = 1$.

Fig. 11. (c1) - (c9) Tangential contact forces distributions in all shapes: (c1) - (c3) before shearing before shearing, (c4) - (c6) at peak of $b = 0$, and (c7-c9) at peak of $b = 1$.

4. Fabric Tensor

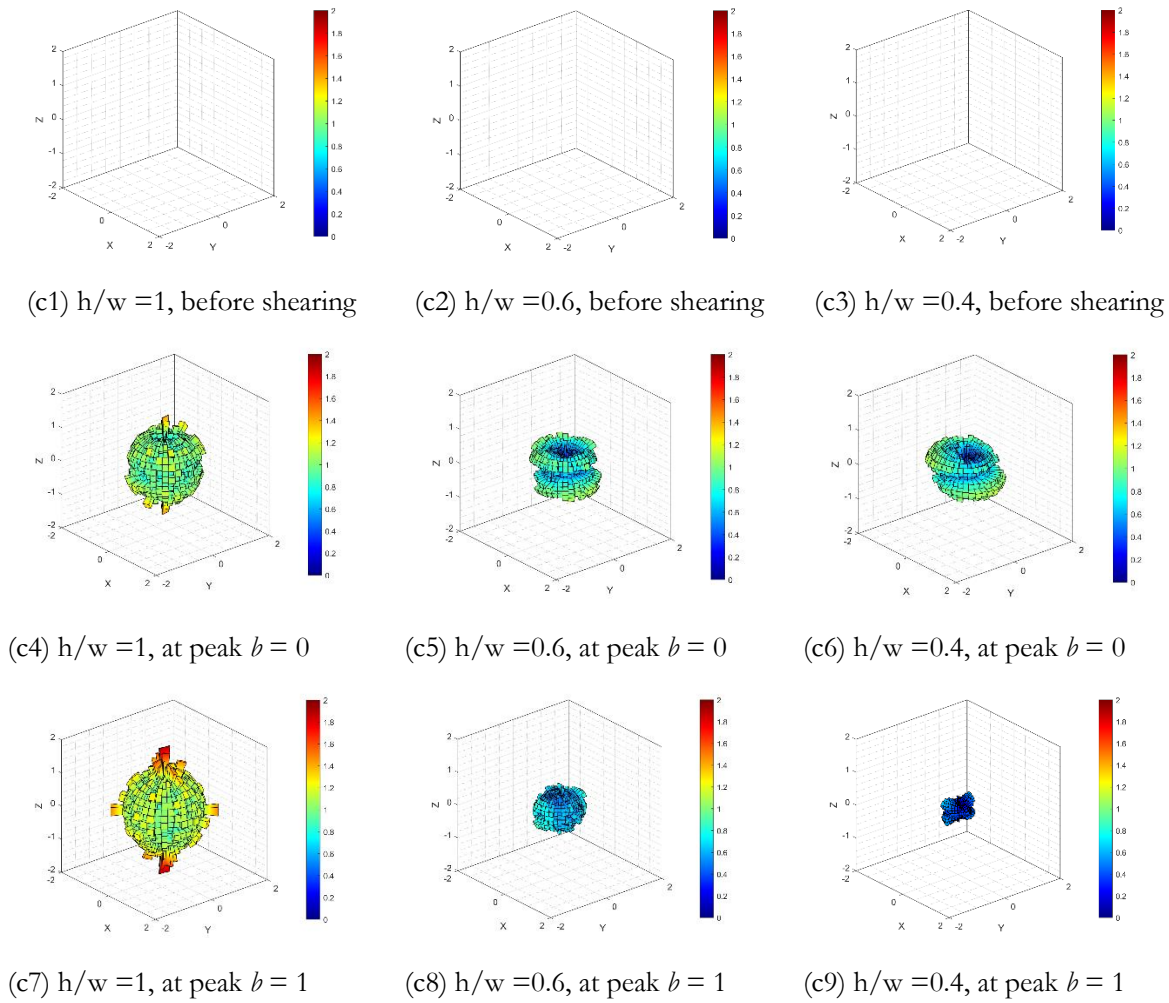Figures 12 (a1)–(c3) shows the evolutions of the principal fabric tensors of h/w = 1, 0.6 and 0.4 indicating the contact intensity in each direction of the principal stresses. The fabric tensor was defined by Oda [23] as one of the key factors to indicate the strength of macro behavior. The fabric tensor is:

$$F_{ij} = \frac{1}{M} \sum_{k=1}^{M} n_i^k n_j^k \qquad (5)$$

where M is the total number of contacts, n_i^k is the part of unit vector n^k. F_{ZZ}, F_{XX}, and F_{YY} are the principal values of fabric tensors in major, intermediate, and minor directions. In Fig. 12(a1), F_{ZZ} of h/w = 1(sphere) increases when $b = 0$ and decreases after b increases. As for Fig. 12(a2), F_{XX} decreases when $b = 0$ and gradually increases after b increases. In Fig. 12(a3), F_{YY} begins to decrease when $b = 0$ and keeps decreasing after b increases. Similarly, Huang et al. [13], Zhou et al. [15] and [17]

reported that the principal fabric tensor showed the similar trend as those of the stress tensor in the true triaxial tests. In Fig. 12(b1), F_{ZZ} of h/w = 0.6 increases in the similar degree of all b. In Fig. 12(b2), F_{XX} gradually decreases when $b = 0$ but it increases when $b = 0.3, 0.5, 0.7$ and 1. The trend of b increases together with F_{XX}. In Fig. 12(b3), F_{YY} begins to decrease in all b but keeps decreasing when b increases. In Fig. 12(c1), F_{ZZ} of h/w = 0.4 increases when b increases. This shows the opposite trend to F_{ZZ} of h/w = 1. It can be seen that the particle h/w = 1 when $b = 1$, F_{ZZ} decreases with the increase of b (see Fig. 12(a1)) while h/w = 0.4 shows the opposite trend (see Fig. 12(c1)). It is noted that F_{ZZ} should increase in the maximum degree under stress path $b = 0$. This should have occurred when the particle is h/w = 1 or sphere, but it does not happen in the particle h/w = 0.4. Thus, the contact orientations of particle h/w = 0.4 affects the increasing trend of the intermediate stress ratio b. Namely, the contact orientations of particle h/w = 0.4 before shearing is more anisotropic than h/w = 0.6 while h/w = 1 is isotropic assembly.
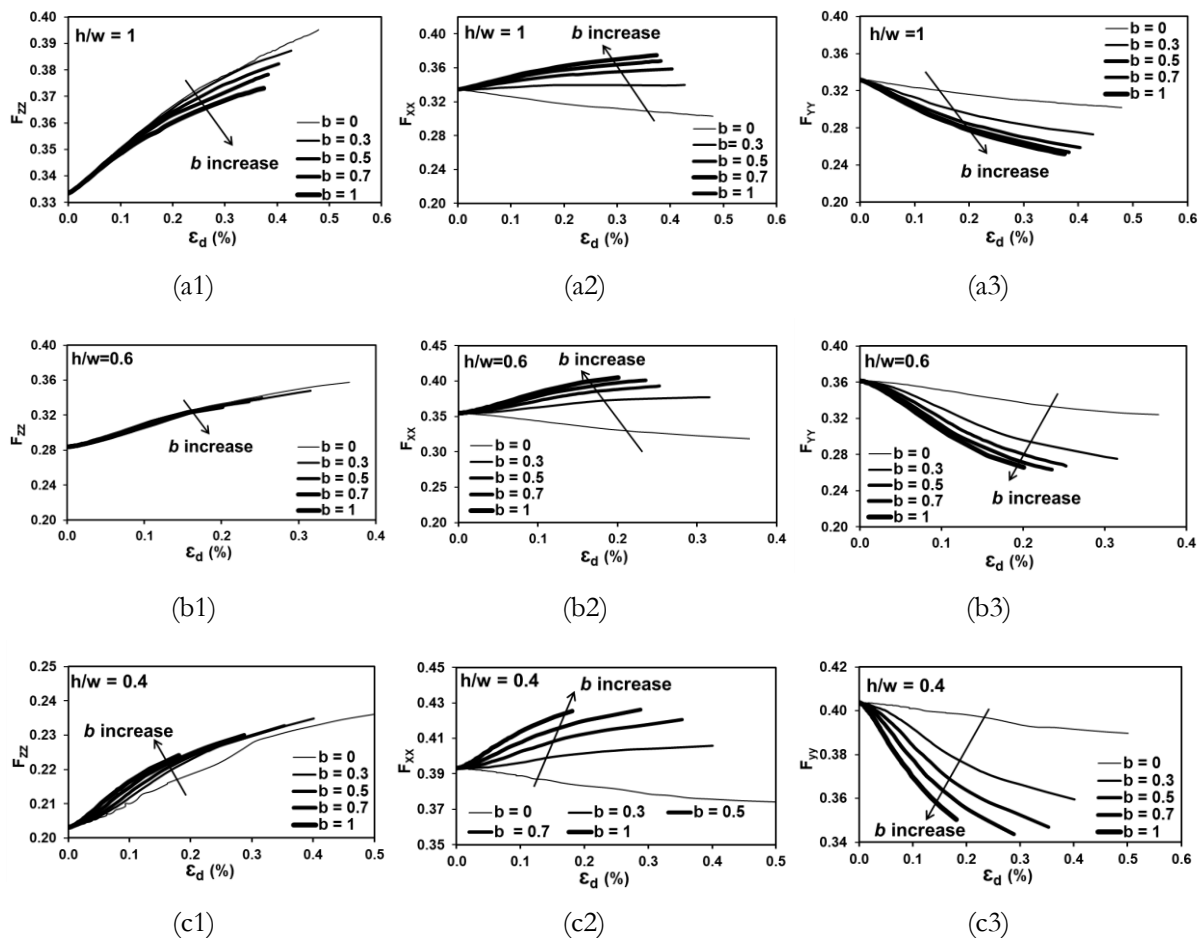

Fig. 12. (a1)–(c3) Principal fabric tensors of all samples.

5. Deviatoric Anisotropy Coefficient Evolutions

The deviatoric mechanical anisotropy mainly resulted from loading stress paths and depends greatly on the generated internal contacts. The internal contacts induced the contact force and related to the contact plane's orientation of each particle. As usual, the anisotropy of the contact normal as well as the branch vector can describe the geometrical anisotropy of the assemble. The anisotropy coefficients can be identified to be normal contact force anisotropy and tangential contact force anisotropy. The deviatoric invariants representing the contact normal anisotropy, normal and tangential contact forces anisotropies are defined to quantify anisotropy's degree. The tensor explains the magnitudes of normal contact forces without considering the degree anisotropy of contact orientation. The coefficient of anisotropy tensors, a_{ij}^r, a_{ij}^n and a_{ij}^t were resulted from their invariants in the same way as the stress tensor [9, 15, 25, 26, 32, 33]. The a_{ij}^n can also be described is:

$$a_{ij}^n = \frac{15}{2} \frac{F'^n_{ij}}{\bar{f}_0^n} \tag{6}$$

The shape of the average normal contact forces was created from the approximate equation similar to the distribution of fabric. The equation is:

$$\bar{f}^n(\Omega) = \bar{f}_0^n \left[1 + a_{ij}^n n_i n_j \right] \tag{7}$$

The a_{ij}^t is:

$$a_{ij}^t = \frac{15}{3} \frac{F_{ij}^t}{\bar{f}_0^n} \tag{8}$$

The coefficients of the deviatoric anisotropy a^r, a^n, a^t can be described as:

$$a^r = \sqrt{\frac{3}{2} a_{ij}^r a_{ij}^r} \tag{9.1}$$

$$a^n = \sqrt{\frac{3}{2} a_{ij}^n a_{ij}^n} \tag{9.2}$$

$$a^t = \sqrt{\frac{3}{2} a_{ij}^t a_{ij}^t} \tag{9.3}$$

The evolution between the coefficients of the deviatoric anisotropy a^r, a^n, a^t and the equivalent deviatoric strain ε_d (%) for all shapes under different b values are shown in Figs. 13(a1)–(c3). Figure 13(a1) shows that the a^r increase together with b increase. It maximizes when $b = 1$. The less a^r means less deviatoric in contact normal of particles. The large a^r means greater deviatoric. In Figs. 13(b1) and (c1), a^n and a^t increase together with b decrease. a^n shows the high influence on b because it shows the similar trend with the curve between stress ratio and equivalent deviatoric strain in Fig. 4(a). Figures 13(a1),

(a2) and (a3) shows a^r of spherical h/w = 1, ellipsoid h/w = 0.6 and 0.4. Figure 13(a2), it can be seen that a^r of h/w = 0.6 starts at 1 but decreases and increases with an increase of ε_d (%). In Fig. 13(a3), a^r of h/w = 0.4 shows the maximum in the beginning but decrease.in the end. This means that the sample h/w = 0.4 shows the most anisotropic behaviors followed by h/w = 0.6 and h/w = 1 (spherical particles). Obviously, the h/w = 1 is isotropic sample, and h/w = 0.6 and 0.4 are anisotropic samples. Moreover, it can be seen in Figs. 13(a1), (a2) and (a3) that b value depends on the particle orientations and the particle shapes. Then, Figs. 13(b1), (b2) and (b3) show a^n of sphere particle h/w = 1, ellipsoid h/w = 0.6 and 0.4. Figure 13(b3) shows that a^n of h/w = 0.4 shows the maximum start from 5 but then it increases together with the decrease of b. Figure 13(b2) shows that a^n of h/w = 0.6 starts from 2 but then it increases together with the decrease of b. The a^n of h/w = 1 in Fig. 13(b1) starts from 0 and then increases together with the decrease of b. Then, Figs. 13(c1), (c2) and (c3) shows a^t of sphere particle h/w = 1, ellipsoid h/w = 0.6 and 0.4. The a^t of all samples starts from 0 but increased together with the decrease of b. Thus, the evolution of a^r, a^n, a^t of isotropic samples, h/w = 1, and anisotropic samples, h/w = 0.6 and 0.4, depend on the shape of particle, but on b.

6. Conclusions

The study aims to review various mechanical behaviors of 3 different shapes, h/w (height/width) equal to 0, 0.6 and 0.4). 8,000 particles with h/w = 0 were formed into spherical particle assemblies but h/w = 0.6 and 0.4 were formed into ellipsoidal particle assemblies. The stress path $b = 0, 0.3, 0.5, 0.7$ and 1 were used to learn the effect of various intermediate principal stress. The results of macro mechanical and microscopic behaviors including the contact force and deviatoric anisotropy characteristics of all particle shapes were reported. The conclusions are followed:

1. The ellipsoidal particles h/w = 0.4 and 0.6 were inherent anisotropy where the spherical particles h/w = 1 were isotropic in all directions before shearing. The stress-strain curves showed that the strains of ellipsoidal particles h/w = 0.4 and 0.6 show extension first, followed by compression but spherical particles showed compression in the beginning. To conclude, the spherical particles were dense samples in all directions of principal stresses, but ellipsoidal particles were loose samples. This resulted from the fact that the shape, even the preparation of the samples, were in the same condition.

2. The coordination number and sliding contract fraction of ellipsoidal particles h/w = 0.4 were greater than h/w = 0.6 and h/w = 1 (spheres). So, the ellipsoidal shape caused contacts and sliding particles more than the spherical particles even in the same number of particles.

3. The forces chain of normal contact forces could be used in the 3 dimensions of contact distributions to draw pictures and show the anisotropic level of the

granular materials. Most contact force distribution was aligned with the direction in major loading stress.

4.   The ellipsoidal particles h/w = 0.4 showed the highest level of anisotropic, followed by h/w =0.6 but spheres h/w =1 was isotropic. The distributions in normal contact forces changed depending on stress paths and intermediate stress ratio b.

5.   The fabric tensor and the deviatoric anisotropy coefficient could be used to give the mechanical response of spherical particles of granular soils. But the deviatoric anisotropy coefficient was not used to give the mechanical response of non-spherical particles.
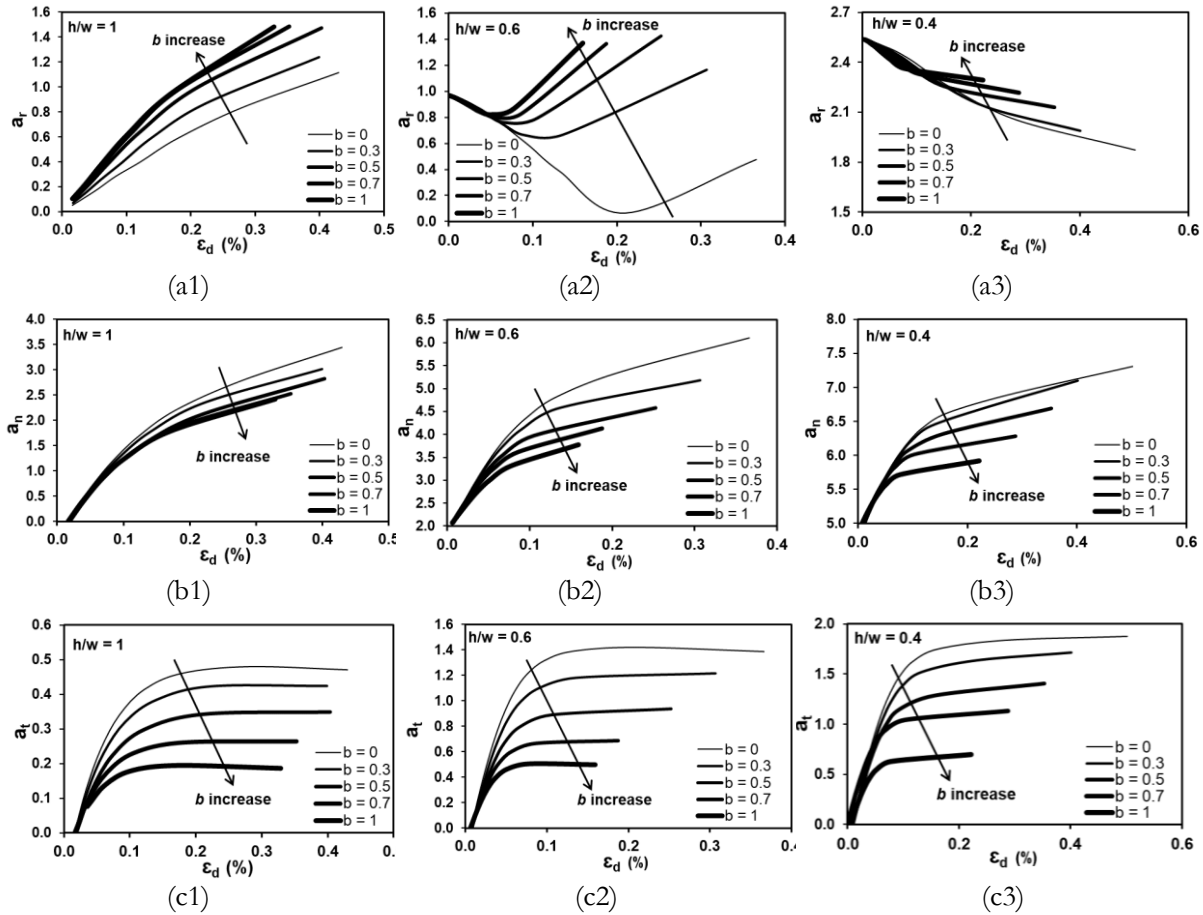
Figs. 13 (a1) – (c3) The relationship of a^r, a^n, a^t and ε_d (%) in all samples.

References

[1]   Z. Huang, Z. Yang, and Z. Wang, "Discrete element modeling of sand behavior in a biaxial shear test," *J. Zhejiang Univ. Sci. A*, vol. 9, pp. 1176–1183, 2008. [Online]. Available: https://doi.org/10.1631/jzus.A0720059.

[2]   I. Cavarretta, M. Coop, and C. O'sullivan, "The influence of particle characteristics on the behavior of coarse grained soils," *Géotechnique*, vol. 60, no. 6, , pp. 413–423, 2010.

[3]   Z. X. Yang, J. Yang, and L. Z. Wang, "Micro-scale modeling of anisotropy effects on undrained behavior of granular soils," *Granul. Matter.*, vol. 15, no. 5, pp. 557–572, 2013.

[4]   G. C. Cho, J. Dodds, J. Dodds, and J. Santamarina, "Particle shape effects on packing density, stiffness, and strength: natural and crushed sands," *J. Geotech. Geoenviron. Eng.*, vol. 132, no. 5, pp. 591–602, 2006.

[5]   P. V. Lade, "Assessment of test data for selection of 3-D failure criterion for sand," *Int. J. Numer. Anal. Meth. Geomech.*, vol. 30, no. 4, pp. 307–333, 2006.

[6]   Y. Xiao, Y. Sun, H. Liu, and F. Yin, "Critical state behaviors of a coarse granular soil under generalized stress conditions," *Granul. Matter.*, vol. 18, no. 2, pp. 1–13, 2016.

[7]   P. A. Cundall and O. D. L. Strack, "A discrete numerical model for granular assemblies," *Géotechnique*, vol. 29, no. 1, pp. 47–65, 1979.

[8]   M. Oda, "Deformation mechanism of sand in triaxial compression tests," *Soils and Foundations*, vol. 12, no. 4, pp. 45–63, 1972.

[9]   R. J. Bathurst, "A study of stress and anisotropy in idealized granular assemblies," Ph.D. Thesis, Queen's University, Kingston, Canada, 1985.

[10] T. G. Sitharam, "Micromechanical modeling of granular materials: Effect of confining pressure on mechanical behavior," *Mech. Mater.*, vol. 31, no. 10, pp. 653–665, 1999.

[11] T. G. Sitharam, S. V. Dinesh, and N. Shimizu, "Micromechanical modelling of monotonic drained and undrained shear behaviour of granular media using three-dimensional DEM," *Int. J. Numer. Anal. Meth. Geomech.*, vol. 26, no. 12, pp. 1167–1189, 2002.

[12] M. Sazzad, K. Suzuki, and A. Modaressi-Farahmand-Razavi, "Macro-micro responses of granular materials under different *b* values using DEM," *Int. J. Geomech.*, vol. 12, no. 3, pp. 220–228, 2012.

[13] X. Huang, K.J. Hanley, C. O'Sullivan, C.Y. Kwok, and M. A. Wadee, "DEM analysis of the influence of the intermediate stress ratio on the critical-state behavior of granular materials," *Granul. Matter.*, vol. 16, no. 5, pp. 641–655, 2014.

[14] D. Phusing, K. Suzuki, and M. Zaman, "Mechanical behavior of granular materials under continuously varying *b* values using DEM," *International Journal of Geomechanics*, vol. 16, no. 1, p. 04015027, 2015.

[15] W. Zhou, J. Liu, G. Ma, et al. "Three-dimensional DEM investigation of critical state and dilatancy behaviors of granular materials," *Acta Geotech.*, vol. 12, pp. 527–540, 2017.

[16] Y. Liu, D. Zhang, S. Wu, and P. Yu, "DEM investigation on the evolution of fabric under true triaxial conditions in granular materials," *International Journal of Geomechanics*, vol. 20, p. 04020110, 2020.

[17] C Nouguier-Lehon, B. Cambou, and E. Vincens, "Influence of particle shape and angularity on the behaviour of granular materials: a numerical analysis," *Int. J.Numer.Anal. Methods Geomech.*, vol. 27, no. 14, pp. 1207–1226, 2003.

[18] Y. H. Xie, Z. X. Yang, D. Barreto, and M. D. Jiang, "The influence of particle geometry and the intermediate stress ratio on the shear behavior of granular materials," *Granul. Matter.*, vol. 19, no. 2, pp. 1-13, 2017.

[19] M. R. Kuhn, *OVAL and OVALPLOT: Programs for Analyzing Dense Particle Assemblies with the Discrete Element Method.* University of Portland, 2006. Accessed: Mar 12, 2023. [Online]. Available: http://faculty.up.edu/kuhn/oval/doc/oval_0618.pdf

[20] C. Thornton, "Numerical simulations of deviatoric shear deformation of granular media," *Géotechnique*, vol. 50, no. 1, pp. 43–53, 2000.

[21] M. Kuhn, "Smooth convex three-dimensional particle for the discrete-element method," *J. Eng. Mech.*, vol. 129, no. 5, pp. 539–547, 2003.

[22] J. Wang, H. S. Yu, P. Langston, and F. Fraige, "Particle shape effects in discrete element modelling of cohesive angular particles," *Granul. Matter*, vol. 13, no. 1, pp. 1–12, 2011.

[23] M. Oda, "Fabric tensor for discontinuous geological materials," *Soils Found.*, vol. 22, no. 4, pp. 96–108, 1982.

[24] W. Zhou, L. F. Yang, G. Ma, and X. L. Chang, "Macro-micro responses of crushable granular materials in simulated true triaxial tests," *Granular Matter*, vol. 17, no. 4, pp. 497–509, 2015.

[25] K. Chantawarangul, "Numerical simulations of three dimensional granular assemblies," Ph.D. Thesis, University of Waterloo, Waterloo, Ontario, Canada, 1993.

[26] T. G. Sitharam, S. V. Dinesh, and N. Shimizu, "Micromechanical modelling of monotonic drained and undrained shear behaviour of granular media using three-dimensional DEM," *Int. J. Numer. Anal. Meth. Geomech.*, vol. 26, no. 12, pp. 1167–1189, 2002.

[27] T.-T. Ng, "Shear strength of assemblies of ellipsoidal particles," *Géotechnique*, vol. 54, no. 10, pp. 659–669, 2004.

[28] L. Rothenburg, "Micromechanics of idealized granular systems," Ph.D. Thesis, Carleton University, Ottawa, Ontario, Canada, 1980.

[29] L. Rothenburg and R. J. Bathurst, "Analytical study of induced anisotropy in idealized granular materials," *Géotechnique*, vol. 39, no. 4, pp. 601–614, 1989.

[30] L. Rothenburg, and R. J. Bathurst, "Micromechanical features of granular assemblies with planar elliptical particles," *Geotechnique*, , vol. 42, no. 1, pp. 79–95, 1992.

[31] Y. Yamada and K. Ishihara, "Anisotropic deformation characteristics of sand under three dimensional stress conditions," *Soils Found.*, vol. 19, no. 2, pp. 79–94, 1979.

[32] Y. Zhang, S. Deng, V. Le, and Y. Sun, "Micro-mechanism of the intermediate principal stress effect on the strength of granular materials," *Soil Behavior and Geomechanics*, pp. 465–475, 2014.

[33] J. Tian, E. Liu, L. Jiang, X. Jiang, Y. Sun, and R. Xu, "Influence of particle shape on the microstructure evolution and the mechanical properties of granular materials," *Comptes Rendus Mécanique*, vol. 346, no. 6, pp. 460-476, 2018, doi: 10.1016/j.crme.2018.03.006.

Daraporn Phusing is a lecturer at faculty of Engineering at Sriracha, Kasetsart University, Thailand. She received a B.Eng. degree in civil engineering from Kasetsart University (2001), and a Ph.D. degree in Science and Engineering from Saitama University, Japan (2015). Her research interests in simulation of soil behaviors using FEM and DEM.

Pulpong Pongvithayapanu is an assistant professor at the faculty of Engineering at Sriracha, Kasetsart University, Thailand. He received B.Eng. and M.Eng in civil engineering from Sirindhorn International Institute of Technology, Thammasat University (1996, 1999), and a Ph.D. in civil engineering from Chulalongkorn University (2010). His research interests are geotechnical earthquake engineering, the behavior of recycled material in a soil mixture, application of FEM in geotechnical engineering.

Udomporn Tungkasiri is a lecturer at faculty of Science at Sriracha, Kasetsart University, Thailand. He received a B.Sc. degree in agriculture (1995), and a M.Sc. degree in Information Technology from from Kasetsart University, Thailand (2000). His research interests in data science, database, file management, information technology, protocol and computer communications.

Porjan Tuttipongsawat is a lecturer at the Faculty of Engineering at Sriracha, Kasetsart University, Thailand. She received a B.Eng. degree in Civil Engineering from Chulalongkorn University (2011), M. Eng and a Ph.D. degree in Civil Engineering from Tokyo Institute of Technology, Japan, in 2014 and 2019, respectively. Her research interests are Solid Mechanics, Vibration-based Damage Detection, and Structural Health Monitoring.